Dynamics of Polar Vortex Crystallization

S. Rijal,[1,*] Y. Nahas,[1,*] S. Prokhorenko,[1,†] and L. Bellaiche[1,2]

[1]Smart Ferroic Materials Center, Physics Department and Institute for Nanoscience and Engineering, University of Arkansas, Fayetteville, Arkansas 72701, USA

[2]Department of Materials Science and Engineering, Tel Aviv University, Ramat Aviv, Tel Aviv 6997801, Israel

(Received 14 February 2023; revised 7 August 2023; accepted 9 July 2024; published 29 August 2024)

Vortex crystals are commonly observed in ultrathin ferroelectrics. However, a clear physical picture of origin of this topological state is currently lacking. Here, we show that vortex crystallization in ultrathin $Pb(Zr_{0.4}, Ti_{0.6})O_3$ films stems from the softening of a phonon mode and can be described as a $Z_2 \times SU(1)$ symmetry-breaking transition. This result sheds light on the topology of the polar vortex patterns and bridges polar vortices with smectic phases, spin spirals, and other modulated states. Finally, we predict a resonant switching of the vortex tube orientation driven by midinfrared laser light which could enable new technologies.

DOI: 10.1103/PhysRevLett.133.096801

Periodic repetition of polar vortex tubes were predicted to form in atomically thin $Pb(Zr, Ti)O_3$(PZT) films [1,2] and observed at room temperature in $PbTiO_3/SrTiO_3$(PTO/STO) superlattices [3]. These emergent states, hereon referred to as vortex crystals (VC), can be controlled by several tuning factors [4–7] and are researched for their technologically prominent properties, such as collective vortexon excitations [8,9], coupling to light [10] and electrons [11]. Apart from perfectly periodic crystalline arrangements, vortex tubes were also shown to form glass- and liquidlike phases. Namely, Nahas *et al.* [12] have recently shown that out-of-equilibrium cooling of ultrathin ferroelectric films can result in meandering vortex tube arrangements named polar labyrinths. These phases are characterized by a well-defined vortex tube structure at the local scale and a short-range ordering of vortex tubes but lack the long-range periodicity of vortex crystals. The same study revealed glasslike dynamical properties of polar labyrinths—a low temperature (T) kinetic arrest and dynamical re-organization of the vortex tubes at finite temperatures was predicted and observed in ultrathin PZT and $BiFeO_3$ films [12]. These finding allowed for the discovery of an inverse transition linking polar labyrinths and VCs. Finally, Zubko *et al.* [13] presented numerical evidence of thermally activated motion of polar vortices in PTO/STO superlattices reminiscent of a melting process. Such VC to a vortex liquid transition was recently studied by Gómez-Ortiz *et al.* [14].

The discoveries of polar vortex crystals, glasses, and liquids pose an interesting question about the nature of mesoscale ordering of polar vortices. These states have been recently shown to share a profound connection with polar bubbles [4,6,7,11,12] which is similar to the relation between wavelike spin states (e.g., conical or helical phases) and magnetic bubbles or skyrmions. Moreover, the established link [4] between vortex freezing and phase separation kinetics clearly showed that the formation of vortex patterns is intimately related to symmetry breaking. If so, what are the symmetries involved? Do vortex tubes behave as particles or shall rather be seen as "condensed" waves? And, finally, can answering these questions allow for a better understanding of vortex crystals, liquids, and labyrinths and lead to a prediction of new phenomena?

Here, we answer all these questions using effective Hamiltonian molecular dynamics simulations [2,15–18] of $PbZr_{0.4}Ti_{0.6}O_3$ (PZT) films. Technically, Newtonian dynamical equations are solved for all the variables which are local soft modes (proportional to local dipoles), inhomogeneous and homogenous strain variables. Predictor-corrector integrator algorithm is implemented to integrate equations of motion with the integration time step being 0.5 fs (1 MD step). System equilibration is done at constant pressure and temperature (NPT ensemble) where the temperatures of all structural degrees of freedom are controlled by the Evans-Hoover thermostat [19]. At any chosen temperature, the system is first equilibrated for 50 000 MD steps, and further simulation is performed to obtain any static or dynamical properties. Our analysis of the finite temperature lattice excitations reveals that the melting of VC is associated with the softening of a phonon mode at a wave vector away from the Brillouin zone center. Furthermore, the identified mode acquires a Goldstone character associated with an emergent $Z_2 \times SU(1)$ continuous symmetry at the transition temperature T_C. These results clarify the symmetry breaking mechanism and provide a new interpretation of the polar vortex states as

*S. R. and Y. N. contributed equally to this letter.

†Contact author: prokhorenko.s@gmail.com

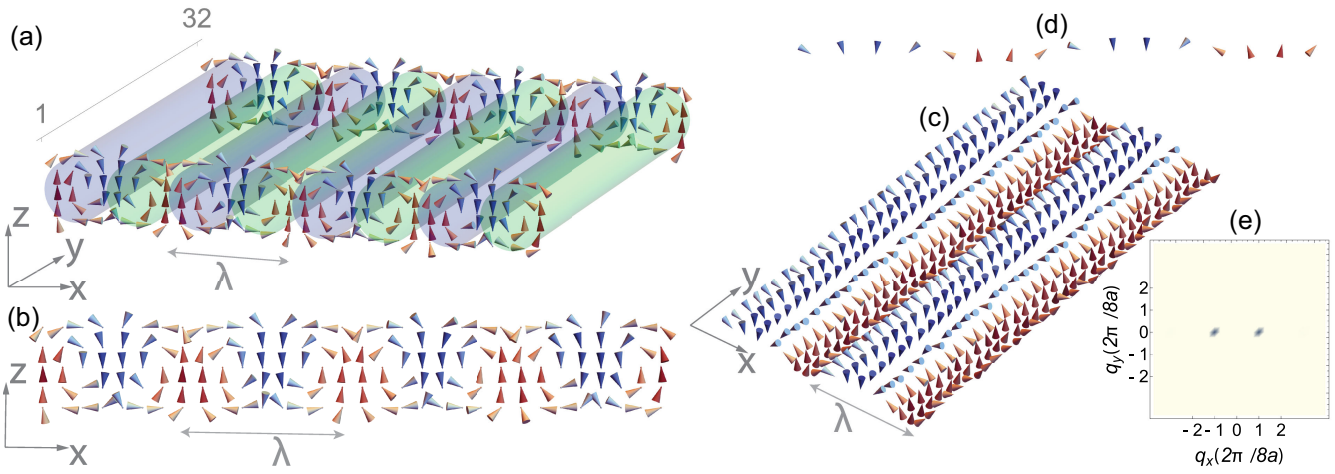

FIG. 1. (a) VC state at 25 K, averaged over 50 ps. Vortices are seen on the xz faces (only $y = 1$ and $y = 32$ planes are shown). Blue (green) tube represents clockwise (anticlockwise) vortex tube; (b) and (c), respectively, show a xz ($y = 8$) and xy ($z = 4$) plane, with only two stripe periods shown, of the supercell where cycloidal periodic modulation of x and z components of dipoles is seen along the x direction with a period of length $\lambda \sim 8a$. (d) Dipoles along a straight line (line of intersection of $z = 4$ and $y = 1$ planes). (e) Structure factor, S_q, obtained by taking 2D Fourier transform of the z components of the dipoles in (c).

waves akin to spin spirals, charge density waves, and density modulations in liquid crystals. Finally, the proposed physical interpretation enables us to predict and numerically confirm a new phenomenon—the resonant switching of the vortex crystal orientation with low-amplitude ac fields.

We start by examining the structure of polar vortex crystals, and perform simulations of 5-unit cell (~2 nm) thick PZT films (see methods in Supplemental Material [20]). Such films mimic an epitaxially grown sample under a misfit strain of −2% and have partially screened interfaces with 80% reduction of the surface bound charges. The supercell, initially thermalized at 800 K, is cooled down to 25 K at the steps of 25 K. In accordance with previous studies [2,3,28,29], our simulation show that the film undergoes a phase transition from a paraelectriclike state to a vortex crystal at $T_C \sim 369$ K.

In Fig. 1(a), we show a typical calculated structure of such VC state at $T = 25$ K obtained by averaging over 50 ps (100 000 time steps). The corresponding polar pattern is a periodic repetition of clockwise-anticlockwise vortex tubes formed by local electric dipoles. The axes of such tubes are parallel either to the x or y in-plane directions ($[100]_{\text{p.c.}}$ or $[010]_{\text{p.c.}}$ crystallographic axis, respectively) with the vortices forming in the (x, z) [respectively, (y, z)] cross sections of the film [Fig. 1(b)]. Either of the two equivalent orientations of vortex tubes is chosen at the transition. In this particular simulation, we obtain vortex tubes extending along the y axis and stacked in the x direction.

When looking at the (x, y) cross section of the film [e.g., Fig. 1(c)], the local dipoles form alternating stripes of "up" ($+z$, red) and "down" ($-z$, blue) pointing dipoles. Originating from the difference in the two perspectives, i.e., that of vortices seen in the (x, z) plane and stripes seen in the (x, y) plane, the VC states were previously referred to as polar vortices [3] or stripe domains [1]. However, a close look also reveals that the electric dipoles in all (x, y) planes exhibit a noncollinear modulation with a period of $\lambda \sim 8$ unit cells. Particularly, in Fig. 1(c), one can clearly see a cycloidal wave in the $z = 4$ plane wherein the dipoles exhibit Néel rotations upon traversing the "stripes" as highlighted in Fig. 1(d). This fact is also mirrored in the amplitude S_q of the Fourier transform of the z component of local dipoles shown in Fig. 1(e). The only nonzero S_q values are seen along the x direction corresponding to a wave vector of magnitude $q_x = (2\pi/8a)$, which proves a harmonic wave character of the pattern. Hence, the polar structure in the $z = 4$ plane perfectly matches the distribution of spins in spin cycloids [30,31]. Similar observations have been also made from STEM imaging of vortex crystals in $PbTiO_3/SrTiO_3$ superlattices [32]. However, in the latter case, the dipole modulations also possess an additional Bloch [33] component (rotation about the direction of modulation) due to which the wave pattern is rather helical [34,35]. At the same time, one important difference of the polar VC patterns from, e.g., spin cycloids resides in the changing sense of Néel rotation within the bottom and top halves of the film—the dipoles rotate clockwise (anticlockwise) in the top (bottom) layers with increasing x.

Nonetheless, a mere observation of the structure begs clarification on whether the VC state emerges from a collective excitation of electric dipoles similar to how spin cycloids, helices, and skyrmions found in magnetic counterparts result from collective excitations of their spins [36–39]. To gain further insight on this matter we inquired into the phonon excitation spectra of the VC state, and

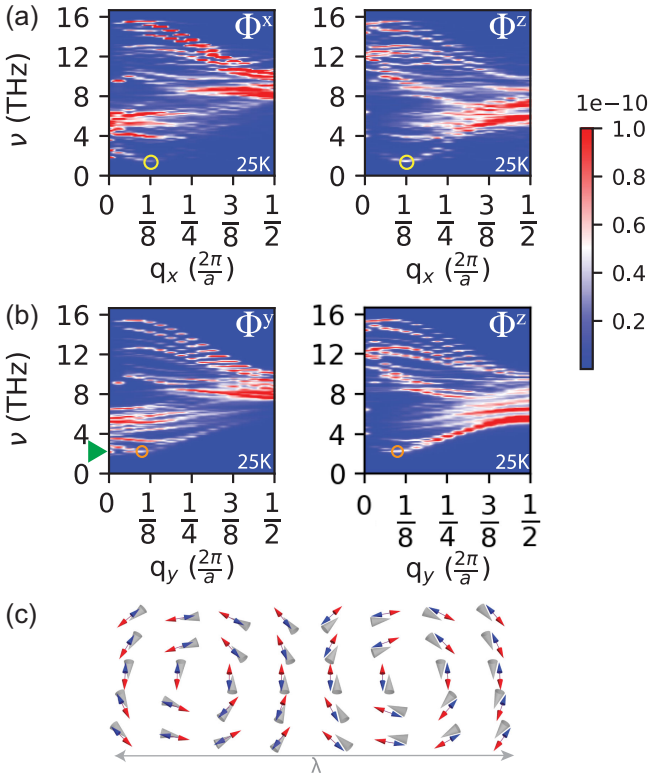

FIG. 2. (a)–(b) SED at 25 K along the [100] and [010] directions. Yellow (orange) circles in highlight the V (competing) mode. Green triangle indicates the lowest frequency mode at Γ. (c) Illustration of the V mode eigenvector where gray (colored) arrows represent static (dynamic) dipole components.

computed the phonon spectral energy density [40,41] (SED) Φ for the simulated vortex crystal shown in Fig. 1(a). Φ is defined as the average kinetic energy of electric dipoles per unit cell at a given wave vector q and frequency ν (see Supplemental Material [20]). We also separate the SED into contributions $\Phi^{\alpha}(\nu, \mathbf{q})$ from the vibration of the $\alpha = x, y, z$ components of the dipoles. Such component-based division of the SED allows us to assess the character of each mode. The component resolved SED calculated at 25 K along the q_x and q_y directions is shown in Figs. 2(a) and 2(b), respectively, for $\alpha = x, y, z$. The lowest frequency polar mode (marked by yellow circles) is revealed in the Φ^x and Φ^z plots along the q_x direction at the wave vector $q_0 = (2\pi/8a)$ corresponding to the periodicity of the VC state. The same mode is not visible in the Φ^y plot (Fig. S1 in Supplemental Material [20]). This indicates that the dipoles fluctuate in the (x, z) plane, which is also the plane of dipolar rotations forming the vortex pattern.

To corroborate this observation, we extract the eigenvector associated with the described mode. Schematically shown in Fig. 2(c), the eigenvector (red or blue arrows) is overlaid with the VC dipolar structure (gray arrows). This mode bears a striking similarity with the VC structure itself. The colored (gray) arrows represent the dynamic (static) component of the dipoles. The lowest energy mode at the $q_x = q_0$ wave vector effectively amounts to the change of the dipole amplitude throughout the material. All of the dipoles first coherently increase in magnitude (red arrows) and then, half a period later, their magnitudes coherently decrease (blue arrows) with the frequency of 1.5 THz. Within the VC state, the mode in question thus describes the oscillation of the amplitude of the VC modulation throughout the material. Recent studies on a $PbTiO_3/SrTiO_3$ system [42,43] with polar vortex ground state also reports a similar eigenvector indicating a similarity in the VC states in PZT and PTO-based systems. Finally, we note the presence of a minimum in the Φ^y and Φ^z plots along the q_y direction [marked by orange circles in Figs. 2(b)]. As we will show below, the corresponding q_y branch is, in fact, a relic of the degeneracy between the x- and y-oriented vortex tube crystals.

We now turn to the behavior of the frequency of the identified vortex mode (V mode) with temperature T. The data obtained from finite temperature MD simulations is shown in Fig. 3(a). Upon increasing the temperature, the frequency of the V mode gradually decreases and approaches zero at $T \sim 369$ K. Such decrease upon approaching the critical temperature T_c is typical of soft

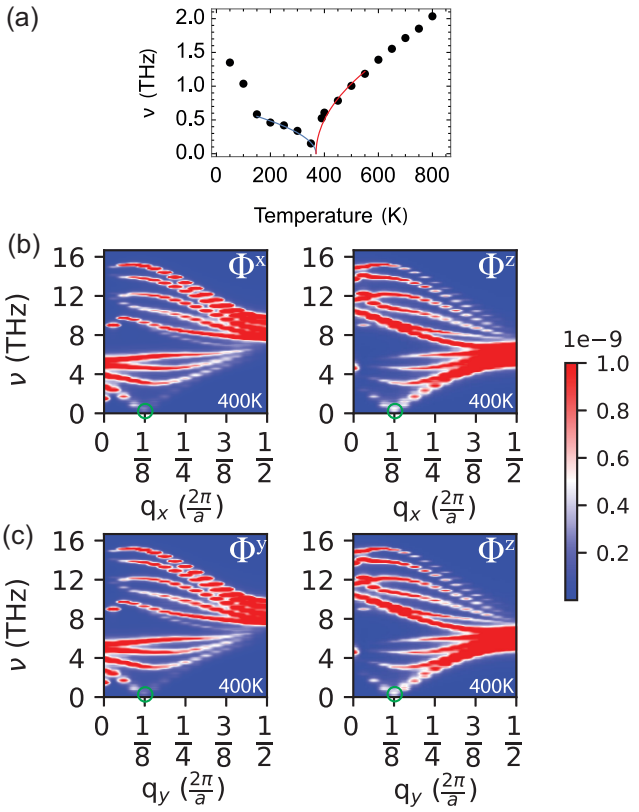

FIG. 3. (a) Temperature dependence of the V mode frequency. (b)–(c) SED at 400 K along the [100] and [010] directions. Green circles highlight the degenerate V modes along the x and y directions.

phonon modes responsible for second-order phase transitions. Furthermore, and as shown by red (blue) fit lines in Fig. 3(a), the softening follows the square root law $\nu \sim \sqrt{|T_c - T|}$ both below and above $T_c \sim 369$ K which is consistent with mean-field approximation of soft mode theory [44]. Similar behavior was previously reported for dynamical formation of vortex tubes in ferroelectric nanowires [45]. For the temperatures approaching T_c from above, a clearly defined polar vortices in the (x, z) planes and wave patterns in the (x, y) planes are not observable. At the first sight, the equilibrium dipolar structure appears to be disordered (e.g., the dipole configuration averaged over 50 ps, i.e., 100 000 time steps at $T = 400$ K is shown in Figs. S3(a)–S3(d) [20]. However, the calculated structure factor [Fig. S3(d)] possesses clear signatures of the periodicity of the VC ground state occurring below T_c. Specifically, $S_{\boldsymbol{q}}$ acquires the shape of a ring with the radius $|\boldsymbol{q}| \sim q_0 = (2\pi/8a)$. The latter observation points to a liquidlike phase consisting of a superposition of the competing long-range ordering modes, but that has not condensed yet along any particular direction.

Figures 3(b) and 3(c) contain the dispersion relations of optical phonons at $T = 400$ K and are representative of the temperature region within the upper vicinity of T_c. Beyond the observation of the softening of the V mode frequency in Fig. 3(a), one can clearly see that the dispersion of the VC branch becomes quasilinear in the vicinity of $q_x \sim q_0$ and $q_y \sim q_0$ [Figs. 3(b) and 3(c)]. Such behavior is typical of gapless Goldstone modes responsible for the breaking of continuous symmetries, which, in our case, corresponds to the translational invariance of the liquid state at $T > T_c$ described by the SU(1) Lie group [20]. The second symmetry involved is a discrete rotational symmetry isomorphic to a cyclic Z_2 group that relates the vortex crystals with tube axis oriented either along the x or y axis. Such symmetry explains why the dispersions along the q_x [Fig. 3(b)] and q_y [Fig. 3(c)] axes are identical up to 90° in-plane rotation of the local dipoles. Above the transition, the V modes with the propagation vector along either $[100]_{\text{p.c.}}$ and $[010]_{\text{p.c.}}$ are indistinguishable and soften upon decreasing the temperature. Then, at $T = T_c$, the system relaxes to either one of the vortex crystal states and, upon further cooling, the previously degenerate V modes split into the two low-frequency excitation branches with similar, yet distinct dispersions [see yellow and orange circles in Figs. 2(a) and 2(b)].

Having corroborated the hypothesis of the wave origin of the polar vortex patterns, we now turn to possible implications of this idea. The competition of two symmetry-related V modes clarifies that the transition can be described by a 2D complex order parameter that we will denote as $\boldsymbol{\mathcal{Q}} = (\mathcal{Q}_x, \mathcal{Q}_y)$ (see methods in Supplemental Material [20]) while the vortex crystallization breaks the $Z_2 \times SU(1)$ symmetry. These observations readily address several open questions. First, the $Z_2 \times SU(1)$ order parameter space clarifies the so-far obscure nature of topological defects in vortex tube states [46]. Particularly, the underlying SU(1) symmetry leads to disclination- and dislocation-like structures [47] while the Z_2 subgroup gives rise to grain boundaries or domain walls. Such walls separate the $\mathcal{Q}_x \neq 0$ and $\mathcal{Q}_y \neq 0$ domains within the polar labyrinth states and are akin to grain boundaries in mosaic glasses [12]. Second, our introduced order parameter allows us to explain the recently observed double-$\boldsymbol{\mathcal{Q}}$ modulated states [48] as a monocliniclike phase with $\mathcal{Q}_x \neq 0$ and $\mathcal{Q}_y \neq 0$ within the same region. Finally, the revealed order parameter reveals new research avenues. Specifically, it establishes that VC states are analogous to quantum spin-1/2 particles and hints at the possibility of switching from a $\mathcal{Q}_x \neq 0$ to a $\mathcal{Q}_y \neq 0$ state below T_c. Such switching could allow us to make an in-plane rotation of the polar vortex tubes in the entire material by 90° and could hardly be imaginable if the VC state was a collection of independent domains or vortex tubes.

Noting that the lowest frequency modes at $\boldsymbol{q} = 0(\Gamma)$ have predominantly in-plane polarization [Figs. 2(a) and 2(b)], it is natural to assume that the VC patterns would be susceptible to in-plane oriented homogeneous electric fields. This observation is also confirmed by recent experiments [9], where an in-plane electric field applied perpendicular to the vortex tube axis switched the zigzag pattern of the displacements of the vortex tubes. To probe the possibility of VC switching, we applied such field oriented along the vortex tube axes (y direction) of the form $E_y(t) = E_0 \sin(2\pi\nu t)$. E_0 is the amplitude of the field while ν denotes its frequency. Figure 4(a) shows a schematic illustration of this computational experiment performed at $T = 25$ K. A particularly remarkable result is obtained when E_0 reaches the threshold value of 50×10^6 V/m and the frequency $\nu \sim 1.92$ THz coincides with one of the low frequency peaks in $\Phi^y(\nu, 0)$ [green triangle in Fig. 2(b)]. Under such conditions, the vortex tubes axes first progressively switch from the y to the x direction, and, at $t > 29$ ps a dynamic vortexonlike [8] oscillation sets in [Figs. 4(b)–4(d)] (video S1 in Supplemental Material [20]). During such oscillation, at first, the radii of the vortices reduce while the clockwise (blue) and the anticlockwise (green) vortex tubes move in the opposite direction along the z axis [Fig. 4(b)]. Such displacements give rise to a dipolar wave that meanders around the vortex tubes and yields a nonzero y component of electric polarization P_y. A static state consisting of such meandering dipolar waves has been reported [10,23,33,49] in different ferroelectric systems. When the field magnitude starts to decrease, the evolution of dipoles reverses and, a quarter of a period later, the system returns to the VC state with tubes extending along the x axis [Fig. 4(c)]. The evolution of the system during the second half period is symmetry equivalent. During this stage, the zigzag vortex tube displacements are

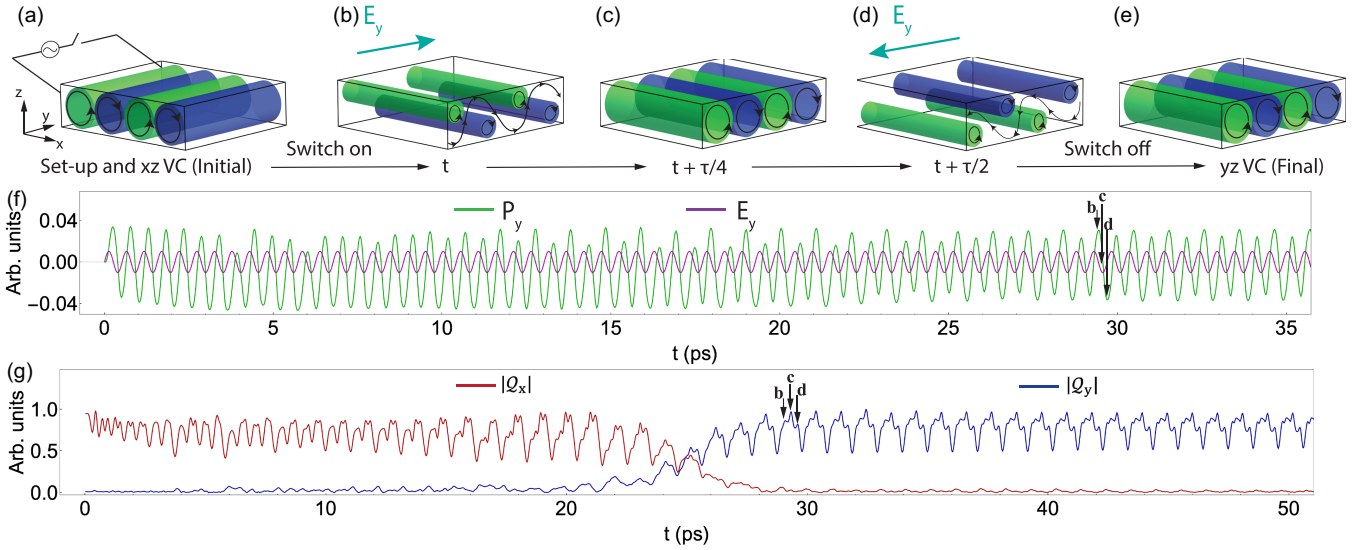

FIG. 4. (a) Schematic diagram depicting VC; evolution of VC on applying electric field along VC axis at times (b) t, (c) $t + (\tau/4)$, (d) $t + (\tau/2)$, and (e) upon switching the field off, where τ is the period of the electric field. (f) The y component of polarization response (green) to the electric field (magenta); rescaled for clarity. (g) Time evolution of the order parameter components $|\mathcal{Q}_x|(t)$ and $|\mathcal{Q}_y|(t)$ of the VC state. Arrows within (f)–(g) are representative of times where states in (b)–(d) occur.

inverted—the clockwise (anticlockwise) vortex tubes displace upwards (downwards) as shown in [Fig. 4(d)]. The direction of the dipolar wave is also reversed resulting in a negative polarization P_y. Upon turning the electric field off, the dipolar pattern settles to the VC state with the vortex axes lying parallel to the x axis which accomplishes the switching [Fig. 4(e)]. The time evolution of P_y overlayed with the applied field $E_y(t)$ is shown in Fig. 4(f). A recent study [9] reported an experiment where a local in-plane electric field applied perpendicular to the vortex tube axis switched the zigzag pattern of displacement of the vortex tubes. However, the switching of the entire vortex crystal remains to be experimentally observed. Such experimental verification can be done by employing linearly polarized infrared laser light to generate the required THz stimulation [50].

Furthermore, the evolution of the order parameter components $|\mathcal{Q}_x|(t)$ and $|\mathcal{Q}_y|(t)$ is shown in Fig. 4(g). These plots clearly demonstrate that, in response to E_y, the initial $|\mathcal{Q}_x| \neq 0$ state (red curve) vanishes and a new $|\mathcal{Q}_y| \neq 0$ state emerges within the time interval $21\ \text{ps} < t < 29\ \text{ps}$. Enroute to switching the axis of the vortex tubes (see video S2 in Supplemental Material [20]), the system passes through some dynamical and topologically nontrivial transient states. Figures S4(a)–S4(d) show several of such dipolar structures including transient vortex tube deformations [Fig. S4(a)] and meron crystals [Fig. S4(b)] akin to the patterns found in PTO/STO systems [48,51], as well as polar labyrinths [4,12] [Figs. S4(c) and S4(d)] featuring polar disclinations [50] and bubblelike [4] geometries.

Notably, the switching between equivalent VC states is not observed for applied field frequencies that deviate from the frequency $\nu \sim 1.92$ THz. Also, the threshold E_0 value of 50×10^6 V/m is an order of magnitude smaller than the critical out-of-plane fields triggering transitions to the bubble and monodomain states in this system [6]. The described switching thus appears to be a resonant phenomenon. Owing to highly anisotropic properties of vortex crystals, the revealed VC reorientation could lead to the design of low-power and ultrafast switches and signal processing devices.

In summary, our results show that vortex crystals in ultrathin ferroelectrics result from the condensation of soft optical phonons and can be perceived as waves rather than ensembles of domains or standalone vortex tubes. Although the noncollinearity in ultrathin ferroelectrics stems from the confining thin-film geometry and it is not an intrinsic property of bulk materials as is often the case in noncollinear magnetic patterns, this finding establishes a link between topological states in ultrathin ferroelectrics with their magnetic counterparts and opens unexpected analogies with other harmonically modulated states. Such change of perspective can push both the theoretical and experimental research on polar topologies along novel inter-disciplinary directions. Finally, our *ab initio* prediction of the low-power resonant switching of the vortex crystal orientation opens conceptually new possibilities for phonon engineering with polar topologies. We hope this discovery will inspire new experiments and guide a search for similar resonant phenomena in noncollinear magnets.

Acknowledgments—We acknowledge the Vannevar Bush Faculty Fellowship (VBFF) Grant No. N00014-20-1-2834

from the Department of Defense, the MURI ETHOS Grant No. W911NF-21-2-0162 from the Army Research Office (ARO) and the MonArk NSF Quantum Foundry supported by the National Science Foundation Q-AMASE-i Program under NSF Award No. DMR-1906383. S. R. also thanks the Ray Hughes Graduate Fellowship (RHGF) awarded from the Physics Department of the University of Arkansas.

[1] B.-K. Lai, I. Ponomareva, I. I. Naumov, I. Kornev, H. Fu, L. Bellaiche, and G. J. Salamo, Electric-field-induced domain evolution in ferroelectric ultrathin films, Phys. Rev. Lett. **96**, 137602 (2006).

[2] I. Kornev, H. Fu, and L. Bellaiche, Ultrathin films of ferroelectric solid solutions under a residual depolarizing field, Phys. Rev. Lett. **93**, 196104 (2004).

[3] A. K. Yadav *et al.*, Observation of polar vortices in oxide superlattices, Nature (London) **530**, 198 (2016).

[4] Y. Nahas, S. Prokhorenko, Q. Zhang, V. Govinden, N. Valanoor, and L. Bellaiche, Topology and control of self-assembled domain patterns in low-dimensional ferroelectrics, Nat. Commun. **11**, 5779 (2020).

[5] Z. Hong *et al.*, Stability of polar vortex lattice in ferroelectric superlattices, Nano Lett. **17**, 2246 (2017).

[6] V. Govinden, S. Rijal, Q. Zhang, D. Sando, S. Prokhorenko, Y. Nahas, L. Bellaiche, and N. Valanoor, Controlling topological defect transitions in nanoscale lead zirconate titanate heterostructures, Phys. Rev. Mater. **5**, 124205 (2021).

[7] Z. Hong and L. Q. Chen, Blowing polar skyrmion bubbles in oxide superlattices, Acta Mater. **152**, 155 (2018).

[8] Q. Li *et al.*, Subterahertz collective dynamics of polar vortices, Nature (London) **592**, 376 (2021).

[9] P. Behera *et al.*, Emergent ferroelectric switching behavior from polar vortex lattice, Adv. Mater. **35**, 2208367 (2023).

[10] V. A. Stoica *et al.*, Optical creation of a supercrystal with three-dimensional nanoscale periodicity, Nat. Mater. **18**, 377 (2019).

[11] K. Du, M. Zhang, C. Dai, Z. N. Zhou, Y. W. Xie, Z. H. Ren, H. Tian, L. Q. Chen, G. Van Tendeloo, and Z. Zhang, Manipulating topological transformations of polar structures through real-time observation of the dynamic polarization evolution, Nat. Commun. **10**, 4864 (2019).

[12] Y. Nahas *et al.*, Inverse transition of labyrinthine domain patterns in ferroelectric thin films, Nature (London) **577**, 47 (2020).

[13] P. Zubko, J. C. Wojdeł, M. Hadjimichael, S. Fernandez-Pena, A. Sené, I. Luk'yanchuk, J.-M. Triscone, and J. Íñiguez, Negative capacitance in multidomain ferroelectric superlattices, Nature (London) **534**, 524 (2016).

[14] F. Gómez-Ortiz, P. García-Fernández, J. M. López, and J. Junquera, Melting of crystals of polarization vortices and chiral phase transitions in oxide superlattices, Phys. Rev. B **105**, L220103 (2022).

[15] I. Ponomareva, I. I. Naumov, I. Kornev, H. Fu, and L. Bellaiche, Atomistic treatment of depolarizing energy and field in ferroelectric nanostructures, Phys. Rev. B **72**, 140102(R) (2005).

[16] I. Ponomareva, I. I. Naumov, and L. Bellaiche, Low-dimensional ferroelectrics under different electrical and mechanical boundary conditions: Atomistic simulations, Phys. Rev. B **72**, 214118 (2005).

[17] I. Ponomareva, L. Bellaiche, T. Ostapchuk, J. Hlinka, and J. Petzelt, Terahertz dielectric response of cubic $BaTiO_3$, Phys. Rev. B **77**, 012102 (2008).

[18] T. Nishimatsu, U. V. Waghmare, Y. Kawazoe, and D. Vanderbilt, Fast molecular-dynamics simulation for ferroelectric thin-film capacitors using a first-principles effective Hamiltonian, Phys. Rev. B **78**, 104104 (2008).

[19] D. J. Evans, W. G. Hoover, B. H. Failor, B. Moran, and A. J. C. Ladd, Nonequilibrium molecular dynamics via Gauss's principle of least constraint, Phys. Rev. A **28**, 1016 (1983).

[20] See Supplemental Material at http://link.aps.org/supplemental/10.1103/PhysRevLett.133.096801 which includes Refs. [21–27] for additional information about the methods and order parameter structure.

[21] B.-K. Lai, I. Ponomareva, I. Kornev, L. Bellaiche, and G. Salamo, Thickness dependency of 180° stripe domains in ferroelectric ultrathin films: A first-principles-based study, Appl. Phys. Lett. **91**, 152909 (2007).

[22] S. K. Streiffer, J. A. Eastman, D. D. Fong, C. Thompson, A. Munkholm, M. V. Ramana Murty, O. Auciello, G. R. Bai, and G. B. Stephenson, Observation of nanoscale 180° stripe domains in ferroelectric $PbTiO_3$ thin films, Phys. Rev. Lett. **89**, 067601 (2002).

[23] A. Schilling, T. B. Adams, R. M. Bowman, J. M. Gregg, G. Catalan, and J. F. Scott, Scaling of domain periodicity with thickness measured in BaTiO single crystal lamellae and comparison with other ferroics, Phys. Rev. B **74**, 024115 (2006).

[24] I. I. Naumov, L. Bellaiche, and H. Fu, Unusual phase transitions in ferroelectric nanodisks and nanorods, Nature (London) **432**, 737 (2004).

[25] Y. Nahas, S. Prokhorenko, L. Louis, Z. Gui, I. Kornev, and L. Bellaiche, Discovery of stable skyrmionic state in ferroelectric nanocomposites, Nat. Commun. **6**, 8542 (2015).

[26] L. Bellaiche, A. García, and D. Vanderbilt, Finite-temperature properties of $Pb(Zr_{1-x}, Ti_x)O_3$ alloys from first principles, Phys. Rev. Lett. **84**, 5427 (2000).

[27] L. Bellaiche, A. García, and D. Vanderbilt, Low-temperature properties of $Pb(Zr_{1-x}, Ti_x)O_3$ solid solutions near the morphotropic phase boundary, Ferroelectrics **266**, 41 (2002).

[28] D. D. Fong, G. B. Stephenson, S. K. Streiffer, J. A. Eastman, O. Auciello, P. H. Fuoss, and C. Thompson, Ferroelectricity in ultrathin perovskite films, Science **304**, 1650 (2004).

[29] D. Sichuga and L. Bellaiche, Epitaxial $Pb(Zr, Ti)O_3$ ultrathin films under open-circuit electrical boundary conditions, Phys. Rev. Lett. **106**, 196102 (2011).

[30] S. R. Burns, O. Paull, J. Juraszek, V. Nagarajan, and D. Sando, The experimentalist's guide to the cycloid, or noncollinear antiferromagnetism in epitaxial $BiFeO_3$, Adv. Mater. **32**, 2003711 (2020).

[31] D. Senff, N. Aliouane, D. N. Argyriou, A. Hiess, L. P. Regnault, P. Link, K. Hradil, Y. Sidis, and M. Braden, Magnetic excitations in a cycloidal magnet: The magnon spectrum of multiferroic $TbMnO_3$, J. Phys. Condens. Matter **20**, 434212 (2008).

[32] F.-H. Gong *et al.*, Atomic mapping of periodic dipole waves in ferroelectric oxide, Sci. Adv. **7**, eabg5503 (2021).
[33] Q. Zhang, L. Xie, G. Liu, S. Prokhorenko, Y. Nahas, X. Pan, L. Bellaiche, A. Gruverman, and N. Valanoor, Nanoscale bubble domains and topological transitions in ultrathin ferroelectric films, Adv. Mater. **29**, 1702375 (2017).
[34] A. R. Damodaran *et al.*, Phase coexistence and electric-field control of toroidal order in oxide superlattices, Nat. Mater. **16**, 1003 (2017).
[35] P. Shafer *et al.*, Emergent chirality in the electric polarization texture of titanate superlattices, Proc. Natl. Acad. Sci. U.S.A. **115**, 915 (2018).
[36] M. Garst, J. Waizner, and D. Grundler, Collective spin excitations of helices and magnetic skyrmions: Review and perspectives of magnonics in non-centrosymmetric magnets, J. Phys. D **50**, 293002 (2017).
[37] T. Weber, J. Waizner, G. S. Tucker, R. Georgii, M. Kugler, A. Bauer, C. Pfleiderer, M. Garst, and P. Böni, Field dependence of nonreciprocal magnons in chiral MnSi, Phys. Rev. B **97**, 224403 (2018).
[38] E. Turgut, A. Park, K. Nguyen, A. Moehle, D. A. Muller, and G. D. Fuchs, Chiral magnetic excitations in FeGe films, Phys. Rev. B **95**, 134416 (2017).
[39] P. Y. Portnichenko *et al.*, Magnon spectrum of the helimagnetic insulator Cu_2OSeO_3, Nat. Commun. **7**, 10725 (2016).
[40] J. A. Thomas, J. E. Turney, R. M. Iutzi, C. H. Amon, and A. J. H. McGaughey, Predicting phonon dispersion relations and lifetimes from the spectral energy density, Phys. Rev. B **81**, 081411(R) (2010).
[41] S. O. Sayedaghaee, S. Prosandeev, S. Prokhorenko, Y. Nahas, C. Paillard, B. Xu, and L. Bellaiche, Domain-wall-induced electromagnons in multiferroics, Phys. Rev. Mater. **6**, 034403 (2022).
[42] H. Aramberri, N. S. Fedorova, and J. Íñiguez, Ferroelectric/paraelectric superlattices for energy storage, Sci. Adv. **8**, eabn4880 (2022).
[43] F. Gómez-Ortiz, H. Aramberri, J. M. López, P. García-Fernández, J. Íñiguez, and J. Junquera, Kittel law and domain formation mechanism in $PbTiO_3/SrTiO_3$ superlattices, Phys. Rev. B **107**, 174102 (2023).
[44] M. E. Lines and A. M. Glass, *Principles and Applications of Ferroelectrics and Related Materials* (Oxford University Press, New York, 2001).
[45] Z. Gui and L. Bellaiche, Terahertz dynamics of ferroelectric vortices from first principles, Phys. Rev. B **89**, 064303 (2014).
[46] J. Junquera *et al.*, Topological phases in polar oxide nanostructures, Rev. Mod. Phys. **95**, 025001 (2023).
[47] P. M. Chalkin and T. C. Lybensky, *Principles of Condensed Matter Physics* (Cambridge University Press, Cambridge, England, 1995).
[48] D. Rusu *et al.*, Ferroelectric incommensurate spin crystals, Nature (London) **602**, 240 (2022).
[49] L. Lu *et al.*, Topological defects with distinct dipole configurations in $PbTiO_3/SrTiO_3$ multilayer films, Phys. Rev. Lett. **120**, 177601 (2018).
[50] X. Chen, P. Karpinski, V. Shvedov, K. Koynov, B. Wang, J. Trull, C. Cojocaru, W. Krolikowski, and Y. Sheng, Ferroelectric domain engineering by focused infrared femtosecond pulses, Appl. Phys. Lett. **107**, 141102 (2015).
[51] Y.-T. Shao *et al.*, Emergent chirality in a polar meron to skyrmion phase transition, Nat. Commun. **14**, 1355 (2023).